

DOI: 10.1002/adem.201600674

Phase Decomposition of a Single-Phase AlTiVNb High-Entropy Alloy after Severe Plastic Deformation and Annealing**

By Benjamin Schuh,* Bernhard Völker, Verena Maier-Kiener, Juraj Todt, Jiehua Li and Anton Hohenwarter

An equiatomic AlTiVNb high-entropy alloy is deformed by high pressure torsion inducing a nanocrystalline microstructure. The samples then are subjected to isochronal heat treatments between 300 °C and 1000 °C. The hardness increase from ≈ 7.4 GPa for the as-processed state to 10.4 GPa for an annealing temperature of 700 °C, while for higher temperatures the hardness starts to decrease. Furthermore, the reduced modulus increases after annealing treatments as well. It will be shown that the unusual annealing response can be related to the formation of intermetallic phases creating a multi-phase nanocomposite material during annealing. The results give new insights into the thermodynamic stability of this alloy, which are also relevant for coarser-grained microstructures.

1. Introduction

High entropy alloys (HEAs) are currently receiving overwhelming attention from the materials science community, demonstrated

by the abundance of papers and events devoted to this topic.^[1–5] On account of their diversity caused by their multi-principle element character and due to the rather loose definitions, the pool of alloys considered to be a HEA is tremendous, although alloys with a multi-phase microstructure are addressed as Constitutionally Complex alloys (CCAs) as a further distinction lately. In fact, only a minority of systems are true single phase alloys with typically face-centered-cubic (fcc)^[6,7] or body-centered-cubic (bcc) structures.^[8,9] Even in that small subset, some alloys decompose to a multi-phase structure upon annealing, see, for instance, ref.^[10–12] An often proposed potential field of application for HEAs in future is the high-temperature regime^[8,13–16] due to their occasionally outstanding specific yield strengths^[17–19] and their proposed sluggish diffusion behavior.^[2,20] In recent years, several alloys containing refractory metals for high-temperature use have been investigated.^[8,13–16] One of the rare single-phase examples is the quaternary, equiatomic AlTiVNb^[21] alloy, showing a bcc-structure in the as-cast state. It features exceptional compressive yield strength up to temperatures of 800 °C and a low density of 5.59 g cm⁻³. In addition, the AlTiVNb alloy also serves as a base for several other HEAs, for example, with the addition of Zr^[19] or Cr,^[22] where second phase precipitation is achieved, which might improve the high-temperature properties further.

Recent studies concerning the thermodynamic stability of HEAs have extended to the nanocrystalline (NC) grain size regime.^[23] It was shown that potential phase decomposition processes during annealing treatments at relatively low temperatures can occur rapidly in NC materials. The fast diffusion kinetics have been rationalized by the abundance of grain boundaries acting as fast diffusion pathways and preferential nucleation sites

[*] B. Schuh, Dr. B. Völker, Dr. J. Todt, Dr. A. Hohenwarter
Department of Materials Physics, Montanuniversität Leoben
and Erich Schmid Institute of Materials Science, Austrian
Academy of Sciences, A-8700 Leoben, Austria
E-mail: benjamin.schuh@unileoben.ac.at
Dr. V. Maier-Kiener
Department of Physical Metallurgy and Materials Testing,
Montanuniversität Leoben, A-8700 Leoben, Austria
Dr. J. Li
Institute of Casting Research, Montanuniversität Leoben,
A-8700 Leoben, Austria

[**] This work was supported by the Austrian Science Fund (FWF) in the framework of Research Project P26729-N19. Parts of this research were carried out at the light source PETRA III at DESY, a member of the Helmholtz Association (HGF). We would like to thank the Helmholtz-Zentrum Geesthacht and in particular Andreas Stark for assistance in using the beamline P07. Further financial support by the Austrian Federal Government (837900) within the framework of the COMET Funding Programme is highly appreciated. We would also like to thank Prof. Reinhard Pippan for the helpful discussions.

This is an open access article under the terms of the Creative Commons Attribution License, which permits use, distribution and reproduction in any medium, provided the original work is properly cited.

in the NC state. Another contributing factor to the enhanced diffusion in severe plastic deformation (SPD) processed materials might be the presence of a high number of deformation-induced vacancies.^[24] Since the observed phase decomposition is of thermodynamic nature and not a sole peculiarity of the NC state, SPD processing offers a pragmatic way to study the thermodynamic stability of a certain HEA. In contrast, the investigation of the same alloy in its coarse-grained state often requires long-term heat treatments in order to achieve the same decomposition behavior.^[10,11]

Based on these ideas the AlTiVNb alloy was at first transformed into a NC state utilizing high-pressure torsion (HPT) processing and subsequently subjected to various heat treatments between 300 and 1 000 °C. The annealed states then were both mechanically and microstructurally investigated in order to determine:

- 1) The effect of SPD processing on the mechanical properties of the AlTiVNb alloy.
- 2) The thermodynamic stability of the equiatomic AlTiVNb system as well as possible microstructural changes occurring during the annealing treatments.

With the indirect approach of investigating the NC state of an alloy, thus having the advantage of accelerated kinetics, the obtained results can provide valuable information on the microstructural stability of the conventionally coarser-grained AlTiVNb HEA. In this way, the results will help to evaluate the alloy's applicability as a high-temperature alloy in future.

2. Experimental Section

Button-shaped ingots (≈20 mm in diameter, ≈10 mm in height) were produced from high-purity elements (>99.99 wt %) using arc melting and then re-melted several times to improve the chemical homogeneity. Small cylinders with a diameter of 8 mm (length ≈10 mm) were processed from the ingots by electrical discharge machining. From these cylinders disks for HPT deformation with 0.8 mm thickness were machined.

The material was processed by quasi-constrained HPT, an in-depth description of this processing technique is given in Pippan et al.^[25] HPT processing was performed at room temperature with a pressure of 7.8 GPa using a rotational speed of 0.2 rotations min⁻¹.

During HPT processing the ideal shear strain γ is given by

$$\gamma = \frac{2\pi rn}{t} \quad (1)$$

where r is the sample radius, t is the sample thickness, and n the number of rotations. For all samples, five rotations were applied resulting in a saturation of grain-refinement at $r > 1$ mm. The deformed samples were subjected to isochronal (1 h) heat treatments performed for temperatures between 300 and 1 000 °C as well as isothermal heat treatments at 700 °C for varying annealing times.

For nanoindentation as well as for investigations performed via scanning electron microscopy (SEM), the samples were ground and polished, first mechanically with SiC paper and then mechano-chemically (OPS). For transmission electron microscopy (TEM) specimen preparation, samples were first ground down to 100 μm, then mechanically dimpled to about 10 μm and finalized using Ar ion-milling.

The microstructure was studied by employing a SEM (Zeiss 1525) and a TEM from Philips (CM12), which was used for conventional bright field imaging and to obtain electron diffraction pattern images. An image-side Cs-corrected JEOL 2100F was further used for scanning-TEM-imaging as well as energy dispersive X-ray spectroscopy (EDX) measurements.

Synchrotron X-ray diffraction (XRD) experiments were performed at the PETRA III beamline at the DESY Photon Science facility using a beam energy of 87.1 keV. The measured transmission diffraction patterns were analyzed using the software FIT2D^[26] and Match!,^[27] utilizing the Crystallography Open Database, PDF-2 as well as the Inorganic Crystal Structure Database. The diffraction pattern of LaB₆ was used as a reference for detector geometry calibration.

For local characterization a platform nanoindenter G200 (Keysight-Tec) equipped with a diamond Berkovich tip, was utilized. Calibrations of tip shape and frame stiffness were performed regularly following the Oliver Pharr method with fused silica.^[28] By using a continuous stiffness measurement (CSM, 45 Hz, 2 nm oscillation amplitude) unit depth dependent local mechanical properties were determined. All nanoindentation experiments were performed in constant strain rate mode and at thermal drift rates of less than 0.1 nm s⁻¹. Hardness and reduced indentation modulus^[28,29] (directly derived from the Sneddon's equation, containing both, the Young's modulus of tip and sample. However, since no information on the Poisson's ratio of the AlTiVNb alloy currently exists in literature no absolute Young's modulus can be evaluated) were determined by constant strain rate indentation (0.05 s⁻¹) to a preset indentation depth of 2 500 nm. The calculated depth dependent mechanical properties were further averaged between 1 500 and 2 000 nm indentation depth.

For strain rate jump tests,^[30] the applied strain rate was abruptly changed in 500 nm intervals. Thermally activated processes then could be quantified by calculating the strain rate sensitivity (SRS) m and activation volume V^* ($V^* = C^* \cdot \sqrt{3} \cdot k_B \cdot T / mH$) instantaneously^[31] from the measured dependence of hardness H on strain rate $\dot{\epsilon}$ directly at the preset jump indentation in order to probe a constant microstructural state (with C^* : constraint factor of 2.8, k_B : Boltzmann constant, T : room-temperature 25 °C). Detailed information on these procedures can be found in the refs.^[31,32]

3. Results

3.1. Microstructural Evolution and Hardness

The as-cast material shows a coarse-grained microstructure (Figure 1a) with grains in the size range of several hundreds of micrometers, exhibiting a dendritic structure. The dendritic

regions are slightly enriched in Nb and interdendritic areas have a higher Al content as EDX-measurements revealed (not shown here).

The hardness evolution as a function of the shear strain is presented in Figure 1b. Two indentations at equivalent positions were made along the radius at intervals of 0.25 mm and averaged. The corresponding shear strains were calculated using Equation 1. The AlTiVNb alloy in its as-cast state has a relatively high hardness of ≈ 6.2 GPa. With an increase in applied strain the hardness increases due to grain refinement. At a shear strain of about 50, a hardness plateau of $\approx 7.4 \pm 0.5$ GPa is reached suggesting a saturation in grain refinement.

The changes in hardness are reflected by the changes in the microstructure. Figure 1c shows the near center region of the disk after $n = 1/4$ rotation, which has experienced almost no shear deformation ($\gamma \approx 0$) but some compressive deformation during loading of the HPT disk. The changes in contrast represent local changes in orientation and additionally some of the original grain boundaries can be detected near the center region. With higher applied strains the deformation starts to localize in shear bands, in which the microstructure is more refined compared to the material outside of the shear

bands (Figure 1d). When the shear strain is increased further the number of bands increases as well, see Figure 1e. For significantly higher applied shear strains of about 50 (which is equivalent to a radial position of ≈ 1 mm after five rotations) and above the microstructure is homogenously refined (Figure 2a) and a microstructural equilibrium state is reached.

3.2. Characterization of the Saturation State

The saturation microstructure was studied more thoroughly using TEM, see Figure 2a. The formation of non-equilibrium grain boundaries during HPT and their characteristic property of exhibiting long-range elastic stresses leads to often poorly discernible structures and boundaries using classical TEM, thus making an exact measurement of the saturation grain size difficult.^[33] However, based on the grains that are clearly visible in dark field imaging, it can be estimated that the saturation grain size of the investigated AlTiVNb-alloy is in the range of 50 nm. In the inset of Figure 2a, the corresponding electron diffraction pattern is shown. All rings fit to a single-phase bcc material with a lattice constant of about 319 pm, which is in agreement with previous reports in the literature, where a lattice constant of 318 ± 3 pm was measured via XRD by Stepanov et al.^[21]

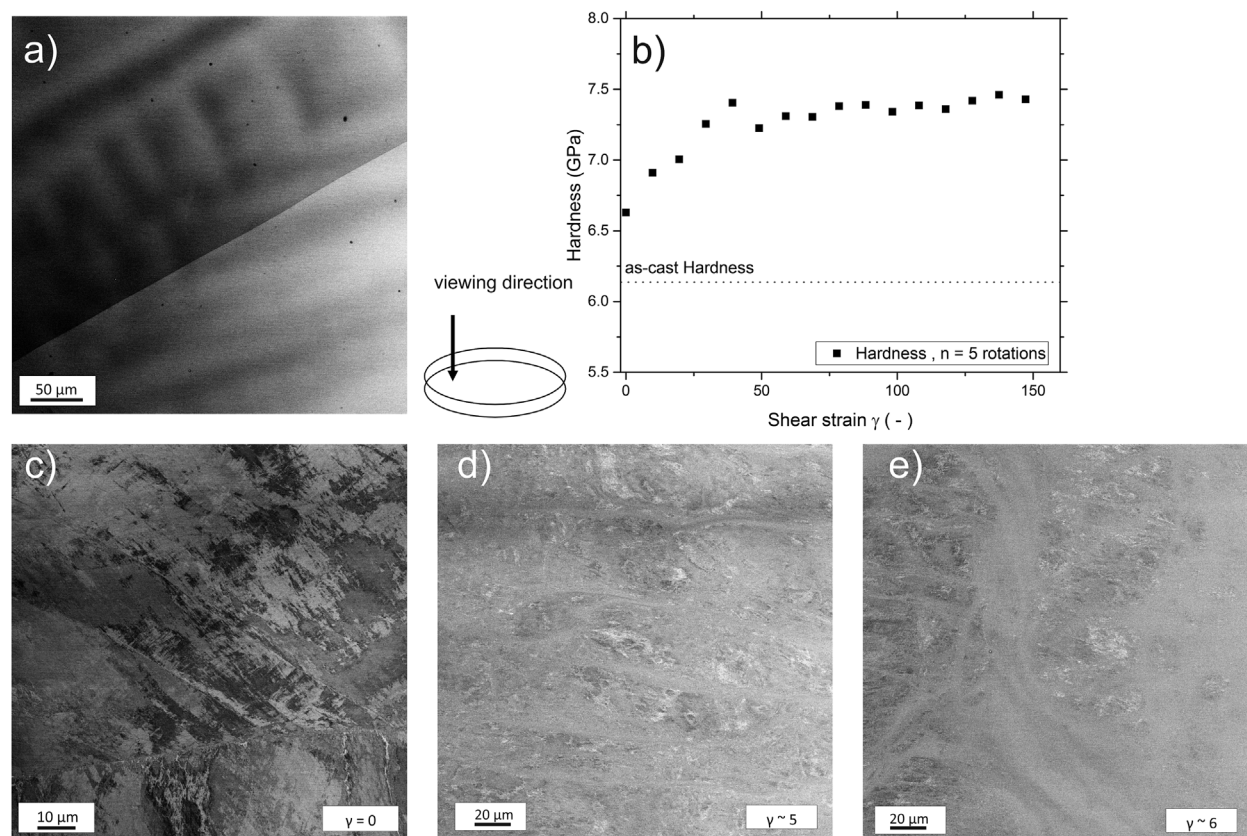


Fig. 1. (a) Low-magnification back scatter electron-micrograph showing the coarse-grained microstructure of the as-cast AlTiVNb high-entropy alloy. The average grain size is in the range of several hundred micrometers and most grains do show a dendritic structure. (b) Hardness evolution as a function of shear strain. A plateau is reached for shear strains larger than approximately 50. (c–e) BSE images taken for different shear strains. (c) Near center region after a quarter rotation, ideally only compressed. (d) For shear strains of about five shear banding commences with a strongly refined microstructure within the bands. (e) Further increase in shear strain, $\gamma \approx 6$, leads to an increase in the number of shear bands and a gradual transformation to a homogeneous NC structure.

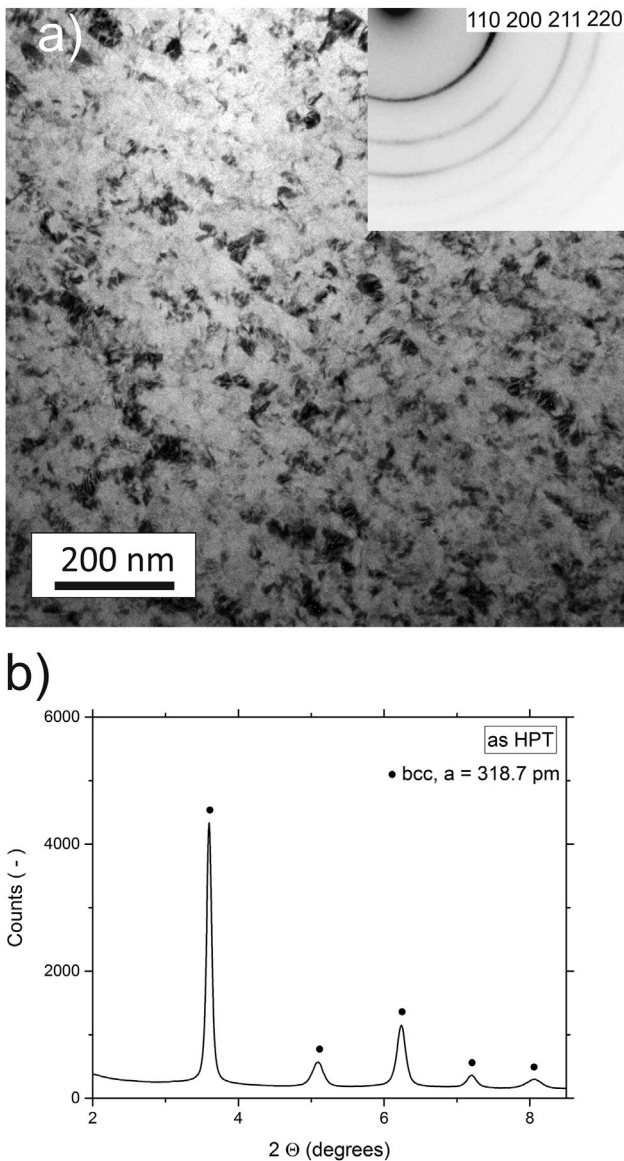


Fig. 2. (a) Bright-field TEM image of the saturation state microstructure. The electron diffraction pattern (inset of a) reveals that the alloy is a single-phase bcc-alloy after HPT processing, which is in agreement with XRD-measurements. (b) The corresponding lattice constant calculated from XRD-measurements of the severely deformed alloy is ≈ 319 pm.

Additionally, it could be revealed that the AlTiVNb alloy retains its single-phase character after HPT deformation by synchrotron XRD measurements (Figure 2b), the corresponding lattice constant for the XRD measurements is ≈ 319 pm. The small discrepancy between the lattice constant measured via XRD compared to the measurements performed by Stepanov et al. can be explained by the fact that the chemistry of the two alloys may not exactly be the same. Additionally, slight inaccuracies in determining the detector-sample distance might also be a possible source of error. In Table 1, the average chemical composition of the HPT deformed material can be seen. Average values and standard deviations were calculated using 50 data points of a line-scan in the saturation region performed by SEM-EDX.

By applying strain rate jump tests, information on thermally activated deformation processes was obtained. For the coarse-grained as-cast state the SRS m is 0.0145 and the activation Volume V^* equals $\approx 11.5b^3$. However, for the nanocrystalline HPT state m increases to 0.019 and V^* drops to approximately $7.15b^3$, see Table 2.

3.3. Annealing Response

Changes in hardness as well as reduced modulus were determined via nanoindentation testing. All values were obtained by averaging the results of six indents, the error bar represent the standard deviation between multiple equivalent indents, see Figure 3.

Even for relatively low annealing temperatures, a significant rise in hardness can be detected, which increases further up to 700°C exhibiting a hardness of about 10.4 GPa. This is a rise of about 3 GPa compared to the HPT state. For higher annealing temperatures, the hardness starts to decrease to about 8.5 GPa for 1000°C .

From the contact stiffness, the reduced modulus of the corresponding annealing states could also be determined. The HPT state has a modulus of approximately 128.3 ± 0.7 GPa, which is significantly lower than the as-cast material with a reduced modulus of about 155.5 ± 5.25 GPa. When the NC material is annealed, the reduced modulus increases as well, reaching a maximum at 800°C (170.8 ± 0.8 GPa). In contrast to the hardness, the modulus shows no significant decrease for higher annealing temperatures of 800°C and above.

In order to determine the causes of the peculiar changes in the mechanical properties during annealing synchrotron XRD measurement were employed. As seen in Figure 4a, for relatively low annealing temperatures up to 500°C no changes in the XRD pattern can be detected. At an annealing temperature of 700°C , the formation of additional peaks can be observed. Besides the original bcc phase the additional peaks suggest the presence of a Nb_2Al phase (Figure 4a and b). Noteworthy is that the peaks for the 700°C specimen are relatively broad. This can be an effect of the NC nature of the additional phase but also a result of the presence of another phase.

For the 900°C sample, the peaks have become narrower and more numerous. While the original bcc high-entropy phase is still present in the material, the peaks corresponding to the Nb_2Al phase have become much more pronounced. Additionally, due to the reduced width of the surrounding

Table 1. Average chemical composition of a HPT processed sample measured via SEM-EDX.

	Chemical composition [at%]
Al	25.3 ± 0.2
Nb	25.7 ± 0.5
Ti	24.5 ± 0.3
V	24.5 ± 0.2

Table 2. Strain rate sensitivity and activation volume for the as-cast and HPT processed sample.

Microstructural state	Strain rate sensitivity m [-]	Activation volume V^* [b^3]
As-cast	0.0145 ± 0.0006	11.50 ± 0.76
HPT	0.0192 ± 0.0011	7.15 ± 0.41

peaks, the partially overlapped peaks in the 700 °C sample are now clearly separated. By reviewing conventional databases and taking into account the possible phases that can form and are known from the binary systems of the four base elements, the development of Ti_3Al seems to be most likely. However, not all peaks can be related to these phases, see Figure 4b, suggesting that an additional phase could be present as well.

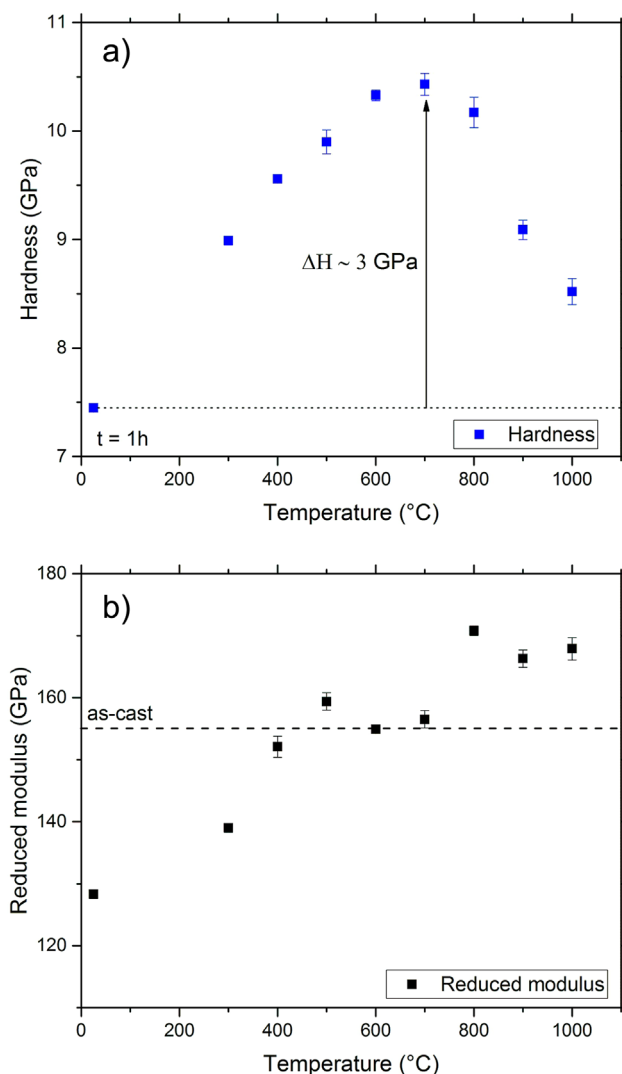


Fig. 3. (a) Hardness evolution during isochronal anneals ($t = 1$ h) for temperatures between 300 and 1000 °C. The hardness reaches a maximum of about 10.4 GPa for an annealing temperature of 700 °C, while for higher temperatures the alloy shows softening. (b) Reduced modulus as a function of temperature. It increases with rising annealing temperatures as well, but unlike for the hardness there is no drop-off for heat treatments above 700 °C.

In order to put these results into perspective TEM-experiments were performed, initially starting with a specimen annealed at 500 °C for 1 h. This complimentary method was chosen, because for XRD-measurements it is known that often volume-fractions of a few vol% are required to be detectable.^[34] Therefore, it is important to investigate the possibility of an onset of precipitation at lower temperatures than 700 °C.

In Figure 5a, the microstructure of a 1-h annealed specimen at 500 °C is presented. In comparison to the HPT state the microstructure appears slightly clearer although grain boundaries overall still seem ill-defined and the annealed specimen shows very little grain growth. The electron diffraction pattern does not show significant changes compared to the as-deformed state, all patterns can still be indexed as the original bcc phase.

The sample annealed at 700 °C for 1 h (Figure 5b) shows much more pronounced changes. The microstructure now appears very clear and there has been noticeable grain growth. More importantly, in the diffraction pattern additional rings are clearly visible, which can be ascribed to a Nb_2Al -phase. Additionally, high-angle angular dark field (HAADF) imaging was performed, revealing darker and lighter regions. Subsequent analysis via TEM-EDX revealed that the lighter regions are distinctly enriched in Nb and Al. (Figure 5c and d). Regarding the possible presence of Ti_3Al in the 700 °C sample, no clear evidence could be found via TEM investigations. For annealing temperatures up to 700 °C, the microstructure remains fine grained, as can be seen in Figure 5b. Higher annealing temperatures lead to a significant increase of the average grain size.

To study the kinetics of the microstructural processes, isothermal heat treatments at 700 °C were additionally performed for 5 min, 1 h, and 15 h (Table 3). Even after just 5 min of annealing the increase in hardness, about 2.6 GPa, is very remarkable, almost reaching the value obtained after the 1 h heat treatment. With a further increase in annealing time to 15 h the hardness continues to increase only slightly.

The reduced modulus shows an equally strong increase within very short term anneals as well, however, with prolonged annealing times the further increase in reduced modulus is much more pronounced compared to increase in hardness, reaching about 176.5 GPa.

After a heat treatment of 800 °C for 1 h, the grains are still in the sub-micrometer regime (Figure 6a), however at the maximum annealing temperature of 1000 °C the grains already have grown to an average size of about 1–2 μm , see Figure 6c. The BSE micrograph of the 1000 °C sample clearly shows lighter and darker regions. By utilizing SEM-EDX line scans it can be qualitatively shown that the lighter regions are again enriched in Nb (Figure 6d), which represents the Nb_2Al phase most likely.

4. Discussion

4.1. Microstructural Development and Homogeneity

The as-cast state of the alloy experiences no homogenization treatment and is therefore chemically inhomogeneous.

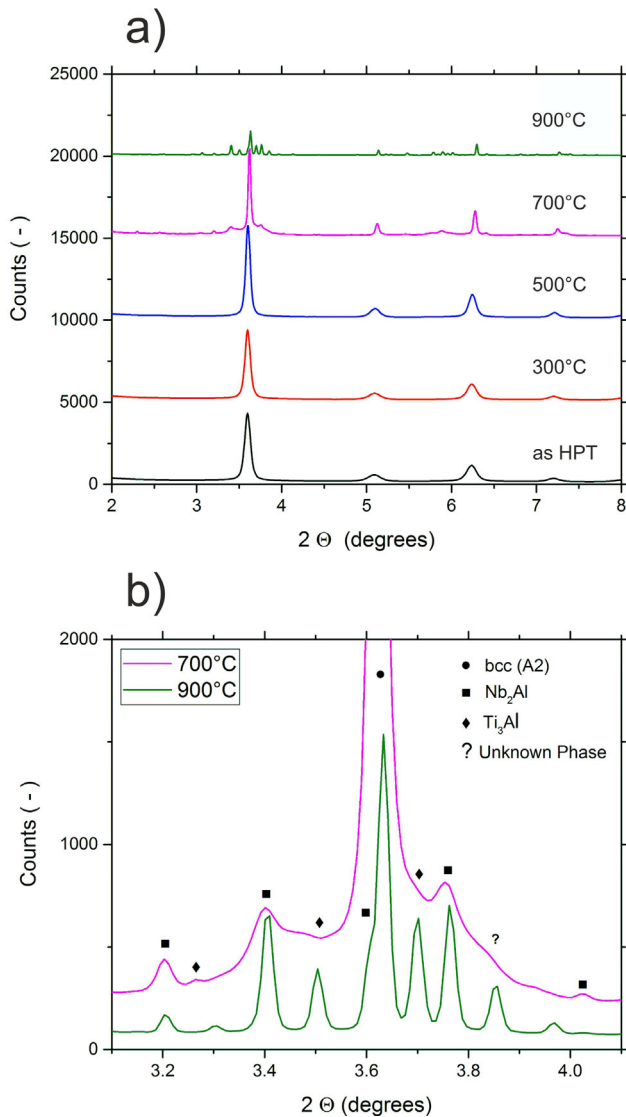


Fig. 4. (a) Synchrotron XRD-measurements imply that the SPD state as well as annealing states up to temperatures of 500 °C for 1 h show no changes in the single-phase bcc structure of the alloy. (b) Further details of (a). For the 700 °C sample additional phases form. For the 900 °C sample the multi-phase structure remains, at least one additional un-indexed peak appears as well. (For interpretation of the references to color in this figure legend, the reader is referred to the web version of this article.)

The high hardness of the coarse-grained as-cast state most likely can be explained by a strong solid-solution hardening effect. In Figure 1a, dendritic areas slightly enriched in elements with high melting point, in this case mostly Nb, and interdendritic regions, which show a somewhat higher Al content, are visible. After HPT processing this chemical inhomogeneity could not be detected by utilizing SEM-EDX anymore. On this length scale, with probing areas in the range of several square-micrometers, homogeneity was achieved. In the literature, chemical homogenization by SPD processing has been reported previously. For instance, Pouryazdan et al.^[35] reported forced chemical mixing in an Ag₆₀Cu₄₀ alloy, where chemical homogenization of the original eutectic microstructure could be achieved by HPT processing. In a similar fashion Quelennec et al.^[36] dispersed 50 nm thick iron filaments into a copper matrix and could show

by means of 3-dimensional atom probe tomography that after 25 rotations via HPT a supersaturated solid solution could be created where the iron was uniformly distributed in the copper matrix.

4.2. Nanoindentation and Strain Rate Sensitivity

At first the trends for the SRS m and the activation volume V^* obtained during nanoindentation (Table 2) testing seem highly peculiar for a single-phase bcc metal. Several authors previously discussed an opposite trend for different bcc-materials investigated by various testing techniques ranging from uniaxial macroscopic testing to multiaxial local testing and for different microstructures. Wei et al.,^[32] for instance, reported a highly reduced SRS after they processed Fe and Ta by severe plastic deformation. Höppel et al.^[37,38] found similar results for Fe and for Cr^[39] and W^[30] also a reduced SRS for the NC states was obtained at room temperature.

Generally, this trend is opposite to that found in fcc materials where an increased SRS is recorded in NC materials. This is mainly discussed in terms of thermally activated dislocation motion and annihilation processes at high angle grain boundaries and moreover in close relationship to a considerably high ductility in these high strength materials. For bcc materials, however, the amount of SRS is directly dependent on the materials specific Peierls stress, which each dislocations has to overcome during deformation and which is strongly dependent on the testing temperature.^[40] However, exemplarily, given the work performed by Maier et al.^[39] for single-crystalline and ultra-fine grained Cr, it could be shown that for testing temperatures of 300 °C this trend was reversed and the SRS started to increase with decreasing grain size, similar to results obtained within this study for AlTiVNb at room-temperature. This behavior was explained that if a certain critical temperature T_c is exceeded thermally activated dislocation-grain boundary interactions start to become more dominant. While for Cr T_c seems to lie somewhere between 100 and 300 °C the observed trend for AlTiVNb might be explained by the fact that T_c might be below or close to room temperature. This idea is also supported by the activation volumes V^* (Table 2). For the as-cast state, a V^* of $\approx 11 \text{ b}^3$ is calculated, showing that thermal activation due to the kink-pair mechanism is still present. This value is also in good agreement with other bcc-metals exhibiting low critical temperatures such as Nb ($T_c \approx 350 \text{ K}$), where at room temperature $V^* \approx 10 \text{ b}^3$ is reported.^[41]

4.3. Annealing Response

Both hardness as well as reduced modulus significantly increase even for very low annealing temperatures (Figure 3), while changes in the microstructure and formation of intermetallic phases could only be observed for annealing temperatures of 700 °C and above (Figure 5b). A strong increase in hardness upon low temperature annealing has been reported for various NC metals and can potentially be explained via dislocation annihilation, since in NC metals there is an abundance of grain boundaries acting as dislocations sinks during annealing. In order to realize plastic

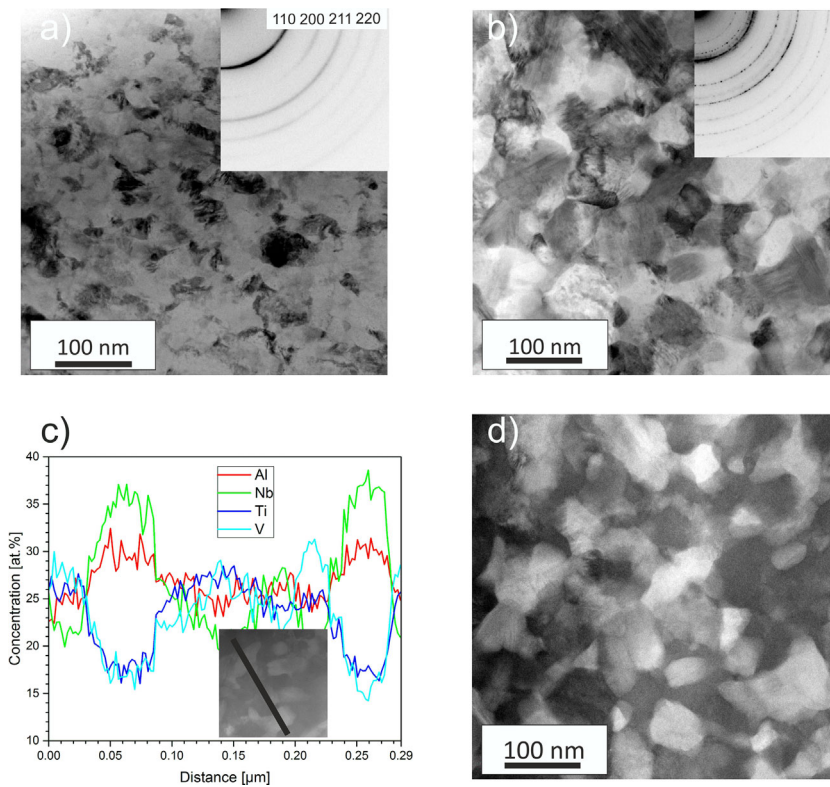


Fig. 5. TEM images of specimens annealed at 500 and 700 °C for 1 h. (a) For the 500 °C sample no additional phases can be detected and the grain boundaries still seem ill-defined. (b) For the 700 °C sample slight grain growth and the formation of additional phases occurs. (c) Line scan indicating that lighter regions are enriched in Nb and Al. (d) A high-angle angular dark-field (Z-contrast) image showing regions being distinctly lighter (Nb-rich) and darker. (For interpretation of the references to color in this figure legend, the reader is referred to the web version of this article.)

deformation after annealing the activation of new dislocations sources might be necessary, which requires high stresses compared to the as-processed state.^[42–44] Another explanation in the literature for the observed hardening is the segregation of solutes to the grain boundaries.^[42,45] A major contribution to the hardening of the alloy especially after annealing at elevated temperatures can be ascribed to the formation of Nb₂Al and possibly Ti₃Al. However, for classical precipitation hardening the precipitates have to be relatively small compared to the grain size. In the present case the newly formed Nb₂Al phase after the 1 h-anneal at 700 °C has a similar size compared to the matrix grains (see Figure 5b and d). Therefore, the composite behavior constraining deformation should be the reason for the

hardness increase. Unfortunately, due to the still relatively small size of the Nb₂Al phase, it was not possible to individually test it. Despite this deficiency the phase is known to have an intermetallic character which is usually associated with high strength.

Along with the increase of hardness, an increase of the reduced modulus was also observed, which can be explained by a composite behavior for higher annealing temperatures where additional phases form. More surprising is the behavior at low temperatures and the difference between the as-cast and the SPD-state (see reduced modulus data point at 20 °C, Figure 3b). The measurements imply a reduction of the modulus through SPD-processing. A decrease of the reduced modulus of NC materials compared to coarse-grained materials has been published frequently.^[46–48] However, it could be often ascribed to inconsistencies of the measuring technique or to the introduction of porosity. Both is very unlikely in the present case. Firstly, the measurements were always performed with the same routine. Secondly, the introduction of porosity during deformation at the presence of high hydrostatic pressures, like in HPT-processing, is not plausible. A possible explanation could be based on a pronounced anelastic behavior of the alloy, which is often attributed to NC metals.^[49]

This explanation in combination with the measuring technique, based on unloading sequences, could possibly lead to the observed reduction of the modulus. With increasing annealing temperature, the defect structure and therefore also the anelasticity would be reduced so that the modulus approaches the value of the coarse-grained state, without showing any indication of grain growth. Another possible explanation is the formation of texture during the HPT processing, which has been reported before in the literature,^[50] thus the decrease in modulus could be explained by a preferred crystallographic orientation that is more compliant. At temperatures around 500 °C the modulus is fully regenerated and the further increase can be associated with the formation of intermetallic phases.

Table 3. Evolution of reduced modulus and hardness as a function of time for isothermal anneals at 700 °C.

Time	Reduced modulus [GPa]	Hardness [GPa]
HPT	128.3 ± 0.7	7.4 ± 0.5
5 min	155 ± 0.6	10.06 ± 0.05
1 h	156.5 ± 1.4	10.43 ± 0.1
15 h	176.5 ± 1.1	10.86 ± 0.03

4.4. Formation of Intermetallic Phases during Annealing

As demonstrated in Figure 4 and 5, the formation of intermetallic phases can be observed via TEM and XRD measurements for specimens annealed at 700 °C for 1 h. Both the diffraction patterns obtained by TEM as well as XRD suggest that the newly formed phase is Nb₂Al. Additional HAADF images in combination with TEM-EDX revealed an enrichment of Nb in certain areas. This is in good agreement with the publication of Stepanov et al.,^[22] where the formation

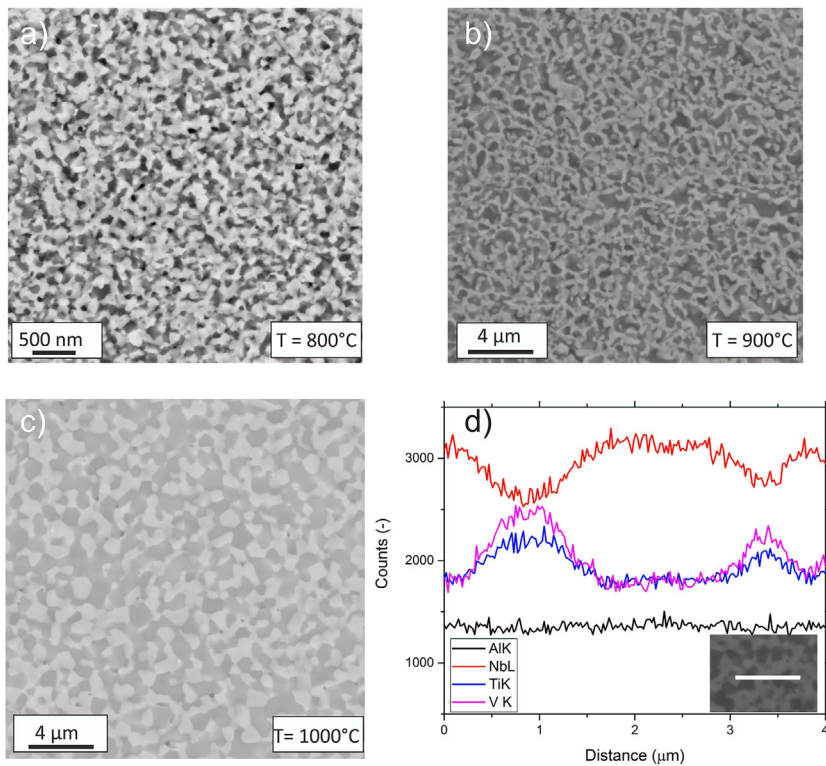


Fig. 6. BSE micrographs of the samples annealed at 800 °C (a), 900 °C (b), and 1000 °C (c) for 1 h. While the average grain size for the 800 °C sample is still in a sub-micrometer regime, for the 1000 °C-anneal the grains have grown to an average grain size of 1–2 μm. d) EDX line-scan performed on a 1000 °C sample showing areas enriched in Nb, which appear lighter in the BSE micrograph. (For interpretation of the references to color in this figure legend, the reader is referred to the web version of this article.)

of an intermetallic phase upon hot deformation of the AlTiVNb alloy at 800 °C as well as 1000 °C was observed and the new phase was determined to be Nb₂Al by means of XRD measurements. Furthermore, according to their thermodynamic simulations the intermetallic phase that should form is Ti₃Al, for annealing temperatures of about 770 °C and below, however the occurrence of such a phase could not be verified experimentally by them. Given the XRD data in Figure 4b, for annealing temperatures of 700 and 900 °C, the formation of a third phase seems to occur. Considering our XRD data and the previous simulation results by Stepanov et al.^[22] it seems likely that the third phase is Ti₃Al. However, subsequent investigations via TEM did not yield a clear proof of the formation of Ti₃Al. A possibility to prove the existence of Ti₃Al in the 700 °C specimen and possibly even more additional phases in the 900 °C sample could be 3-dimensional atom probe tomography measurements in future.

It also has to be considered that the occurrence of Ti₃Al at 900 °C does not match the simulated results by Stepanov et al.^[22] In that regard it has to be noted that prediction of equilibrium phases via Thermo-Calc using the CALPHAD method has yielded results that are often only in partial agreement with experimental results when it comes to HEAs.^[20,51–53] For instance, Zhang et al.^[54] predicted a multi-phase structure for the CrMnFeCoNi alloy correctly at lower temperatures. However, it was experimentally shown^[10,11,23,55] that the single-phase

structure is not restored until about 800 °C, while the CALPHAD results predicted a single-phase structure for temperatures of about 600 °C and above. A main problem of utilizing CALPHAD for HEA systems is that generally available databases often do not extend to the center of the phase diagram. For HEAs, however, the used database should be valid in the entire composition range.^[56] An in-depth description of the challenges of creating such databases can be found in Zhang et al.^[54]

There is a significant shift of the peak-positions in the XRD measurements of the suggested phases between the 700 and the 900 °C sample, see Figure 4. For instance, at $2\theta \approx 3.27^\circ$ the 700 °C sample clearly shows a peak at the position calculated for Ti₃Al, while for the 900 °C sample the peak is shifted to $2\theta \approx 3.3^\circ$. On the other hand at $2\theta \approx 3.5^\circ$ the fit for the 900 °C sample is much better. The intermetallic phase Nb₂Al also contains relatively large amount of “impurities” in the form of Ti and V. This variation in chemical composition certainly should lead to a difference in lattice constant compared to the “pure” phase, therefore, explaining the shifts of the peak positions. Taking this into account, the difference in peak position for Ti₃Al between the 700 and the 900 °C sample can most likely be explained by a variation in their chemical compositions, either because the equilibrium composition for the specific temperatures is different or because the equilibrium composition has not yet been reached after annealing for 1 h. Most likely, both effects contribute to the observed peak shift.

Considering Table 3 it can be seen that, for example, for a heat treatment at 700 °C for 1 h, the material has not reached its equilibrium state yet, since both hardness as well as reduced modulus are further increasing with longer annealing times. A reasonable explanation for the further increase in modulus is the continued formation of secondary phases. The fact that the relative hardness increase for longer annealing times is much less pronounced compared to the modulus change can be rationalized by grain growth which occurs at 700 °C and counteracts the hardness increase gained by additional second phase precipitation.

Assuming that the contribution of the configurational entropy to the overall thermodynamic stability determined by Gibbs free energy decreases along with decreasing temperature, it seems reasonable that some of the observed intermetallic phases should also be stable at much lower temperatures. For these temperatures, the phase decomposition is merely restricted by diffusion kinetics. This seems plausible especially considering that the 700 °C sample apparently does not seem to have reached an equilibrium state after 1 h of annealing despite the accelerated diffusion

kinetics that should occur in NC materials. Therefore, long-term heat treatments to achieve equilibrium states for various temperatures should be a goal of future investigations in order to get a more profound understanding of the thermodynamics of this alloy.

4.5. Feasibility As a High-Temperature Material

Due to its low density and high specific yield strength up to temperatures of 800 °C^[21] AlTiVNb was suggested as a potential material for high temperature applications in future. However, as, for instance, Miracle et al. have pointed out, measuring a single attractive property does not necessarily qualify a material for a certain structural application.^[56] Instead, a multitude of properties such as, for instance, adequate fracture toughness, oxidation resistance, creep, and fatigue behavior as well as long-term microstructural stability are required for practical applications. The latter property, microstructural stability, was investigated in this paper. The result is that the single-phase bcc structure, after casting and subsequent processing via HPT, is not thermodynamically stable. Instead, after an annealing treatment in the temperature range from 700 to 1000 °C a multi-phase microstructure formed and showed an exceptional hardness. While multi-phase structures are usually desired in high-temperature applications, as, for instance, the intermetallic Ni₃Al in Ni-superalloys, these microstructures are highly tailored with regard to size distribution but also, for example, the lattice misfit of precipitates.

HEA development for practical applications nowadays starts to stray away from the single-phase concept^[53,56] in order to gain more favorable properties by second phase precipitation, as Senkov et al.^[15] have recently demonstrated by creating a microstructure similar to those occurring in Ni-superalloys. In our case, however, the multi-phase structure of AlTiVNb, as demonstrated herewith the NC state, merely is a result of phase-decomposition that would likely also occur in its variants with Cr und Zr additions. Thus, long-term microstructural stability of the single-phase bcc state is questionable over a wide temperature range. If the formation of these secondary phases can be tailored to occur in a favorable fashion, AlTiVNb might be a possible candidate for future applications. However, low density and high specific yield strength alone are hardly sufficient and further investigations of other mechanical properties especially in extreme environments need to be performed to determine the feasibility of AlTiVNb as a structural material.

5. Summary and Conclusion

The quaternary, equiatomic AlTiVNb high-entropy alloy was subjected to high pressure torsion, leading to a NC microstructure with an approximate grain size of 50 nm. The NC material was subjected to various heat treatments in order to assess the thermodynamic stability of the alloy. In order to identify changes in the mechanical properties and

microstructure nanoindentation, XRD as well as TEM were employed. The findings can be summarized as follows:

- 1) Information on deformation mechanisms and T_c was obtained by means of nanoindentation for the as-cast as well as the HPT-processed state.
- 2) After isochronal heat treatments of 1 h a strong increase in hardness as well as reduced modulus occurs. Softening of the material commences for annealing temperatures of 800 °C and above.
- 3) Changes in mechanical properties for relatively high annealing temperatures can be explained by formation of intermetallic phases (most likely Nb₂Al and Ti₃Al) and the corresponding creation of a multi-phase-nanocomposite material. For low temperature annealing, a major contribution to the hardness changes might be due to dislocation mediated processes.
- 4) Even for the maximum annealing temperature of 1000 °C, the alloy does not return to its single-phase bcc state.

In conclusion, the AlTiVNb alloy is not thermodynamically stable over an extended temperature range. Even though the formation of intermetallic phases leads to an outstanding hardness of 10.4 GPa, it could also result in a further embrittlement of the alloy, which would be detrimental for room-temperature applications of the NC material. Therefore, ductility and toughness related investigations should be in the scope of future investigations.

Article first published online: January 3, 2017

Manuscript Revised: December 7, 2016

Manuscript Received: September 26, 2016

- [1] Y. Zhang, T. T. Zuo, Z. Tang, M. C. Gao, K. A. Dahmen, P. K. Liaw, Z. P. Lu, *Prog. Mater. Sci.* **2014**, *61*, 1.
- [2] J. W. Yeh, *Ann. Chim. Sci. Des Mater.* **2006**, *31*, 633.
- [3] J. W. Yeh, *JOM* **2015**, *67*, 2254.
- [4] M. H. Tsai, *Entropy* **2013**, *15*, 5338.
- [5] M.-H. Tsai, J.-W. Yeh, *Mater. Res. Lett.* **2014**, *2*, 107.
- [6] B. Cantor, I. T. H. Chang, P. Knight, A. J. B. Vincent, *Mater. Sci. Eng. A* **2004**, *375–377*, 213.
- [7] W. Wang, W. Wang, S. Wang, Y. Tsai, C. Lai, J. Yeh, *Intermetallics* **2012**, *26*, 44.
- [8] O. N. Senkov, G. B. Wilks, D. B. Miracle, C. P. Chuang, P. K. Liaw, *Intermetallics* **2010**, *18*, 1758.
- [9] O. N. Senkov, G. B. Wilks, J. M. Scott, D. B. Miracle, *Intermetallics* **2011**, *19*, 698.
- [10] E. J. Pickering, R. Muñoz-Moreno, H. J. Stone, N. G. Jones, *Scr. Mater.* **2016**, *113*, 106.
- [11] F. Otto, A. Dlouhý, K. G. Pradeep, M. Kuběnová, D. Raabe, G. Eggeler, E. P. George, *Acta Mater.* **2016**, *112*, 40.
- [12] V. Maier-Kiener, B. Schuh, E. P. George, H. Clemens, A. Hohenwarter, *Mater. Des.* **2016**, *115*, 479.
- [13] O. N. Senkov, S. V. Senkova, D. B. Miracle, C. Woodward, *Mater. Sci. Eng. A* **2013**, *565*, 51.

- [14] O. N. Senkov, J. M. Scott, S. V. Senkova, F. Meisenkothen, D. B. Miracle, C. F. Woodward, *J. Mater. Sci.* **2012**, *47*, 4062.
- [15] O. N. Senkov, D. Isheim, D. N. Seidman, A. L. Pilchak, *Entropy* **2016**, *18*, 1.
- [16] J. P. Couzinié, G. Dirras, L. Perrière, T. Chauveau, E. Leroy, Y. Champion, I. Guillot, *Mater. Lett.* **2014**, *126*, 285.
- [17] O. N. Senkov, S. V. Senkova, C. Woodward, *Acta Mater.* **2014**, *68*, 214.
- [18] O. N. Senkov, C. Woodward, D. B. Miracle, *JOM* **2014**, *66*, 2030.
- [19] N. D. Stepanov, N. Y. Yurchenko, V. S. Sokolovsky, M. A. Tikhonovsky, G. A. Salishchev, *Mater. Lett.* **2015**, *161*, 136.
- [20] J. W. Yeh, *JOM* **2013**, *65*, 1759.
- [21] N. D. Stepanov, D. G. Shaysultanov, G. A. Salishchev, M. A. Tikhonovsky, *Mater. Lett.* **2015**, *142*, 153.
- [22] N. D. Stepanov, N. Y. Yurchenko, D. V. Skibin, M. A. Tikhonovsky, G. A. Salishchev, *J. Alloys Compd.* **2015**, *652*, 266.
- [23] B. Schuh, F. Mendez-Martin, B. Völker, E. P. George, H. Clemens, R. Pippan, A. Hohenwarter, *Acta Mater.* **2015**, *96*, 258.
- [24] D. Setman, E. Schafler, E. Korznikova, M. J. Zehetbauer, *Mater. Sci. Eng. A* **2008**, *493*, 116.
- [25] R. Pippan, S. Scheriau, A. Hohenwarter, M. Hafok, *Mater. Sci. Forum* **2008**, *584–586*, 16.
- [26] A. P. Hammersley, S. O. Svensson, M. Hanfland, A. N. Fitch, D. Hausermann, *High Press. Res.* **1996**, *14*, 235.
- [27] CrystalImpact, <http://www.crystalimpact.com/>, **2016**.
- [28] W. C. Oliver, G. M. Pharr, *J. Mater. Res.* **1992**, *7*, 1564.
- [29] W. C. Oliver, G. M. Pharr, *J. Mater. Res.* **2004**, *19*, 3.
- [30] V. Maier, C. Schunk, M. Göken, K. Durst, *Philos. Mag.* **2015**, *95*, 1766.
- [31] K. Durst, V. Maier, *Curr. Opin. Solid State Mater. Sci.* **2015**, *19*, 340.
- [32] Q. Wei, S. Cheng, K. T. Ramesh, E. Ma, *Mater. Sci. Eng. A* **2004**, *381*, 71.
- [33] R. Z. Valiev, R. K. Islamgaliev, I. V. Alexandrov, *Prog. Mater. Sci.* **2000**, *45*, 103.
- [34] M. Birkholz, Principles of X-Ray Diffraction, Wiley-VCH Verlag GmbH & Co. KGaA, Weinheim **2005**.
- [35] M. Pouryazdan, D. Schwen, D. Wang, T. Scherer, H. Hahn, R. S. Averbach, P. Bellon, *Phys. Rev. B Condens. Matter Mater. Phys.* **2012**, *86*, 1.
- [36] X. Quelennec, A. Menand, J. M. Le Breton, R. Pippan, X. Sauvage, *Philos. Mag.* **2010**, *90*, 1179.
- [37] H. W. Höppel, J. May, P. Eisenlohr, M. Göken, *Zeitschrift Für Met.* **2005**, *96*, 566.
- [38] J. May, H. W. Höppel, M. Göken, *Mater. Sci. Forum* **2006**, *503–504*, 781.
- [39] V. Maier, A. Hohenwarter, R. Pippan, D. Kiener, *Scr. Mater.* **2015**, *106*, 42.
- [40] A. Seeger, *Zeitschrift Fuer Met. Res. Adv. Tech.* **1981**, *72*, 369.
- [41] A. S. Schneider, C. P. Frick, B. G. Clark, P. A. Gruber, E. Arzt, *Mater. Sci. Eng. A* **2011**, *528*, 1540.
- [42] E. Ma, T. D. Shen, X. L. Wu, *Nat. Mater.* **2006**, *5*, 515.
- [43] X. Huang, N. Hansen, N. Tsuji, *Science* **2006**, *312*, 249.
- [44] O. Renk, A. Hohenwarter, K. Eder, K. S. Kormout, J. M. Cairney, R. Pippan, *Scr. Mater.* **2015**, *95*, 27.
- [45] R. Z. Valiev, N. A. Enikeev, M. Y. Murashkin, V. U. Kazykhanov, X. Sauvage, *Scr. Mater.* **2010**, *63*, 949.
- [46] H. S. Kim, M. B. Bush, *Nanostruct. Mater.* **1999**, *11*, 361.
- [47] P. G. Sanders, J. A. Eastman, J. R. Weertman, *Acta Mater.* **1997**, *45*, 4019.
- [48] G. E. Fougere, L. Riester, M. Ferber, J. R. Weertman, R. W. Siegel, *Mater. Sci. Eng. A* **1995**, *204*, 1.
- [49] F. Momprou, D. Caillard, M. Legros, H. Mughrabi, *Acta Mater.* **2012**, *60*, 3402.
- [50] A. P. Zhilyaev, T. R. McNelley, T. G. Langdon, *J. Mater. Sci.* **2007**, *42*, 1517.
- [51] C. Ng, S. Guo, J. Luan, S. Shi, C. T. Liu, *Intermetallics* **2012**, *31*, 165.
- [52] A. Manzoni, H. Daoud, S. Mondal, S. Van Smaalen, R. Völkl, U. Glatzel, N. Wanderka, *J. Alloys Compd.* **2013**, *552*, 430.
- [53] E. J. Pickering, N. G. Jones, *Int. Mater. Rev.* **2016**, *61*, 183.
- [54] F. Zhang, C. Zhang, S. L. Chen, J. Zhu, W. S. Cao, U. R. Kattner, *Calphad Comput. Coupling Phase Diagrams Thermochem.* **2014**, *45*, 1.
- [55] N. D. Stepanov, D. G. Shaysultanov, M. S. Ozerov, S. V. Zherebtsov, G. A. Salishchev, *Mater. Lett.* **2016**, *185*, 1.
- [56] D. B. Miracle, *Mater. Sci. Technol.* **2015**, *31*, 1142.